

HYDROVOLTAIC ENERGY HARVESTING FROM NUT SHELLS

NAZMUL HOSSAIN¹, Roozbeh Abbasi¹, Weinan Zhao¹, Xiaoye Zhao¹, Aiping Yu¹, and Norman Y. Zhou¹

¹University of Waterloo

September 19, 2024

Abstract

Water-induced Electric Generators (WEGs) exhibit tremendous promise as sustainable energy sources harvesting electricity through the interaction between materials and water utilizing the hydrovoltaic effect, an innovative green energy harvesting method. However, existing WEG devices predominantly rely on inorganic materials with limited research on naturally available, bio-based materials for hydrovoltaic energy harvesting. This study introduces a novel nutshell-based hydrovoltaic WEG for the first time. This low-cost, organic, and efficient renewable energy source can generate a voltage above 600 mV with a power density exceeding 5.96 $\mu\text{W}\cdot\text{cm}^{-2}$ utilizing streaming and evaporation potential methodologies, which can be sustained for more than a week. Notably, after further chemical treatments and combining the physical and chemical phenomena, output voltage and maximum current density reach a record high of 1.21 V and 347.2 $\mu\text{A}\cdot\text{cm}^{-2}$ respectively, which outperforms most inorganic and organic materials based WEGs. By connecting two units in series and parallel this eco-friendly WEG can power an LCD calculator without the assistance of any rectifier. We believe that this novel nutshell-based WEG provides a significant advancement in WEG technology by offering a sustainable solution for powering electronic devices utilizing agricultural waste.

Article category: Full Paper

Subcategory: materials science, nanotechnology, Batteries, fuel cells, and supercapacitors, Environmental remediation, Devices with multifunctionality

Title: HYDROVOLTAIC ENERGY HARVESTING FROM NUT SHELLS

Nazmul Hossain^{1}, Roozbeh Abbasi¹, Weinan Zhao^{1,2}, Xiaoye Zhao¹,*

Aiping Yu^{1,2,3}, Norman Zhou^{1,3*}*

1. Department of Mechanical and Mechatronics Engineering, University of Waterloo, Waterloo, ON, N2L 3G1, Canada
2. Department of Chemical Engineering, University of Waterloo, Waterloo, Ontario, N2L 3G1 Canada
3. Waterloo Institute for Nanotechnology, University of Waterloo, Waterloo, Ontario, N2L 3G1 Canada

Mr. Nazmul Hossain, PhD student, Department of Mechanical and Mechatronics Engineering, **Dr. Roozbeh Abbasi**, Postdoctoral Fellow, Department of Mechanical and Mechatronics Engineering,

Dr. Weinan Zhao, Postdoctoral Fellow, Department of Chemical Engineering,

Dr. Xiaoye Zhao, PhD student, Department of Mechanical and Mechatronics Engineering, **Professor Aiping Yu**, Director of the Carbon Nanomaterials Laboratory, Department of Chemical Engineering **Professor Norman Zhou**, Canada Research Chair in Advanced Materials Joining and Processing

***Corresponding authors:** nazmul.hossain@uwaterloo.ca; aipingyu@uwaterloo.ca and nzhou@uwaterloo.ca

Keywords: biomaterials, porous materials, water-induced electric generators, green energy harvesting, energy materials

Abstract:

Water-induced Electric Generators (WEGs) exhibit tremendous promise as sustainable energy sources harvesting electricity through the interaction between materials and water utilizing the hydrovoltaic effect, an innovative green energy harvesting method. However, existing WEG devices predominantly rely on inorganic materials with limited research on naturally available, bio-based materials for hydrovoltaic energy harvesting. This study introduces a novel nutshell-based hydrovoltaic WEG for the first time. This low-cost, organic, and efficient renewable energy source can generate a voltage above 600 mV with a power density exceeding $5.96 \mu\text{W}\cdot\text{cm}^{-2}$ utilizing streaming and evaporation potential methodologies, which can be sustained for more than a week. Notably, after further chemical treatments and combining the physical and chemical phenomena, output voltage and maximum current density reach a record high of 1.21 V and $347.2 \mu\text{A}\cdot\text{cm}^{-2}$ respectively, which outperforms most inorganic and organic materials based WEGs. By connecting two units in series and parallel this eco-friendly WEG can power an LCD calculator without the assistance of any rectifier. We believe that this novel nutshell-based WEG provides a significant advancement in WEG technology by offering a sustainable solution for powering electronic devices utilizing agricultural waste.

Introduction

In recent years, the intense focus has been given to finding sustainable energy solutions that are cost-effective and have a minimal environmental impact, and, and are abundant in nature. Several energy harvesting techniques, such as piezoelectricity,^[1] triboelectricity,^[2] thermoelectricity,^[3] have been thoroughly explored to convert mechanical, thermal, and renewable energy into electricity. However, each approach has barriers, such as extensive material costs, complicated preparation procedures, limited resources, and inadequate electrical output, which limit their practical use. It is crucial to maximize the energy extraction from a pure source for long-term feasibility. Because of its abundance (71% of the Earth's surface) and significant intrinsic renewable energy potential, water has gained increasing interest for its use in prominent power generation. While traditional approaches like thermal energy extraction,^[4] or hydroelectricity,^[5,6] generation has been widely exploited, hydrovoltaic method has recently emerged as a viable method for harnessing energy.^[7-10] This unconventional hydrovoltaic system can harness electricity through the direct interaction between functional materials and various forms of water, such as water droplets,^[11] flow of water,^[12,13] wave,^[14,15] evaporation,^[16-19] and moistures.^[20] Evaporation-based energy harvesting from water droplets has recently gained attention in relation to the hydro-voltaic effect.^[7,8] Utilizing the interactions between the water droplet and solid material interfaces, this method can generate electricity by leveraging physical phenomena such as streaming potential,^[21] ionic motion coupling,^[22] triboelectrification.^[23] Since efficient energy harvesting from sustainable sources is crucial, evaporation-driven electrical generators (EEGs) are a potential solution for the progress of renewable energy systems. This EEG process is more spontaneous and can utilize maximum energy from water.^[17] Several novel nanomaterials have garnered significant attention in the realm of hydrovoltaic energy harvesting, which yields electrical potential at the interface between water and a polarizable substance.^[24] Despite the promising characteristics of the novel nanomaterials, such as high conductivity and surface area, their feasibility is limited by their high costs, limited availability, resistance to water flow, and labor-intensive preparation processes. Over the years, naturally available bio-based materials having porous structures were overlooked. Recently, microchannels of different natural wood structures have been exploited for hydrovoltaic energy harvesting.^[25-27] However, most of the existing organic material-based WEGs exhibit lower power density, hindering their suitability for practical device

application. Moreover, the the device size would be substantially larger because of the required shape of the wood^[27] and the required amount of water is considerably higher. On top of that, some forms of pretreatments are required to improve the power density.^[26]In this study, we investigate a new approach—evaporation-driven Water induced Electric generators (WEG) by utilizing natural nutshells, which possess a porous micro/nanochannel structure^[28]and sufficient polar functionalities.^[29] This natural anisotropic 3D micro/nano-channel architecture of nutshells (NSs) facilitates efficient water and nutrient transport.^[30] For the first time, the micro/nanochannels within the NSs (Almond Shell - AS, Filbert Shell - FS, Pecan Shell - PS, Walnut Shell - WS) have been successfully utilized to harness hydrovoltaic energy through evaporation by utilizing the concepts of streaming potential as illustrated in **Figure 1** . A simple one-step preparation process can harvest above 600 mV with a power density of $5.95 \mu\text{W}\cdot\text{cm}^{-2}$. The efficiency of this device is affected by critical factors such as density, porosity, contact area, surface charge, and hydrophilicity. By applying some chemical treatments, the surface area and porosity of the nutshells (NSs) have been augmented. The subsequent highly porous shells exhibit an impressive output potential of 1.21 V and a maximum current density of $347.2 \mu\text{A}\cdot\text{cm}^{-2}$ under the synergistic effect of streaming potential and chemical reactions. These innovative and functional NS-powered energy generators are cost efficient and environmentally friendly, rendering them suitable for powering small electronic devices. Moreover, this innovative technology presents a novel approach to green energy solutions and broadens the range of materials that can be potentially utilized for Water induced Electric Generators (WEGs).

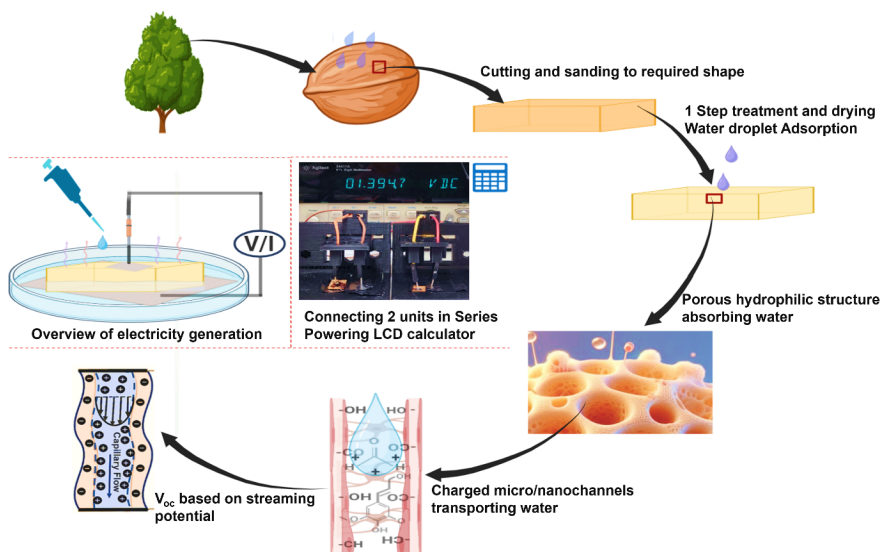


Figure 1: Schematic diagram illustrating the process of an NS-based WEG. The flow diagram illustrates the preparations, porous hierarchical structure, water-surface interactions, water transportation through channels and generating streaming potential. The center left demonstrates voltage/current generation through evaporation in graphite-NS-graphite sandwich structure. A photograph shows two WS- H^+ -WEG devices connected in series; two units in series and parallel can power LCD calculator.

Results and discussion

Physico-chemical properties of nutshells

To observe the microstructural features of the four different types of nutshells (NSs), Almond Shell (AS), Filbert Shell (FS), Pecan Shell (PS), and Walnut Shell (WS), SEM analyses were conducted on the inner

surface, outer surface and the cross sections of the samples. The structure of nutshells reveals a substantial presence of porous tissue with a homogeneous distribution along the structural matrix. These porous tissues form perforations across the layers of the shell facilitating nutrient uptake by allowing the passage of liquids.^[31,32] The ubiquitous distribution of these perforations throughout the shell structure is confirmed by SEM imaging shown in **Figure 2** and **Figure-S 3**. Amongst these four NSs, Almond Shell (AS) and Walnut Shell (WS) exhibit remarkable uniformity in the distribution and arrangement of the apertures pattern, with AS demonstrating larger apertures than the WS. Diameter of these pores ranges from nano to micro scales, traversing both external and internal surfaces. Filbert Shell (FS), and Pecan Shell (PS) exhibit a disorganized distribution of pores (**Figure 2 (d-i)**), ranging from nano to micro scales, facilitating the passage of fluids. Thus, the apertures of these four nutshells act as nano and micro channels for any fluid flow. The configurations of these micro/nanochannels have a variety of geometry including convergent, divergent, and parallel geometrics.^[31-33] Moreover, the abundance of these perforations amplifies the adsorption capacity and augment the surface area for solid liquid interactions enabling faster capillary absorption of water. The composition of nutshells (NS) is primarily consisting of lignin, cellulose, and hemicellulose,^[34,35] which are rich in hydroxyl groups, methoxyl, and carbonyl functional groups.^[36] Therefore, NSs demonstrate mostly hydrophilic and negative surface charges.^[37]

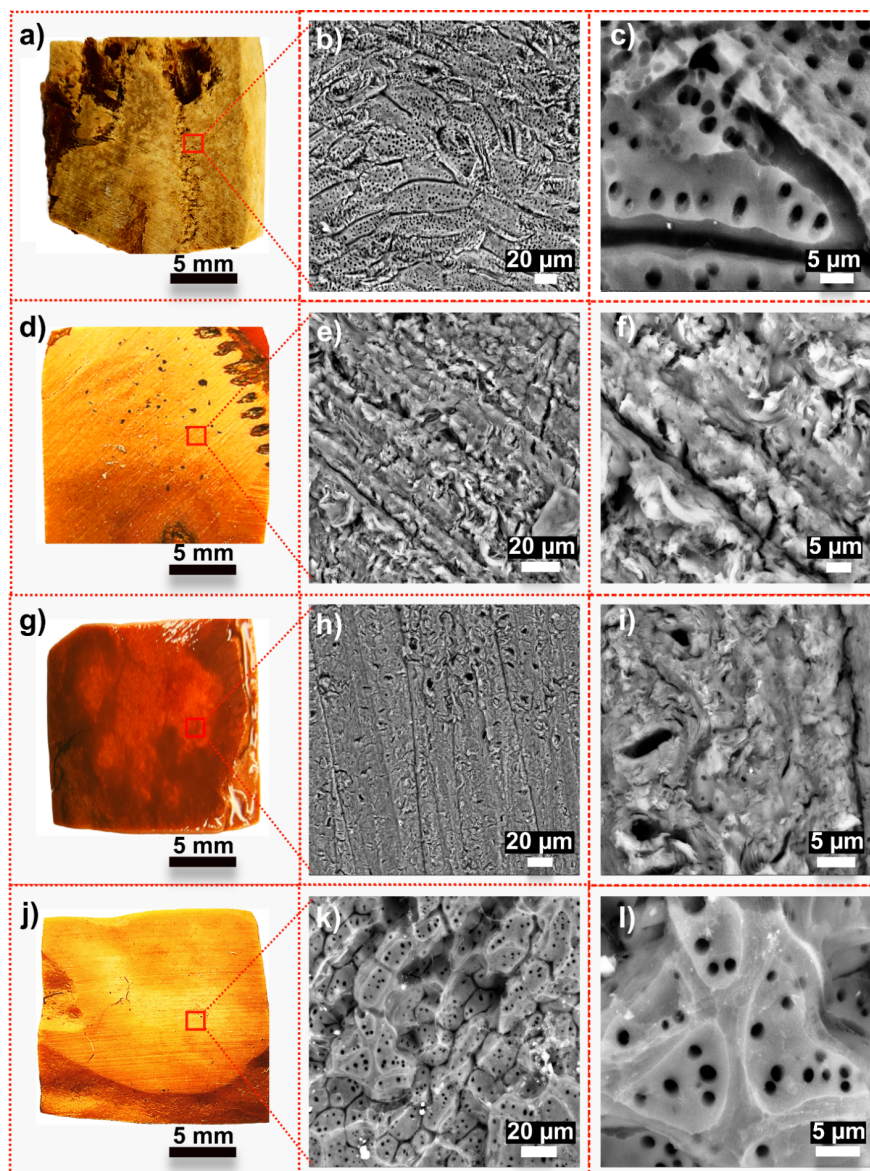


Figure 2: Photograph and SEM images of the four Nutshells (NSs): AS (a, b, c); FS (d, e, f); PS (g, h, i); WS (j, k, l)

Figure 3 (a) shows the Fourier-transform infrared (FT-IR) spectra of four NS samples confirming the presence of the functional groups. All the NSs exhibit distinct peaks at 1033 cm^{-1} , 2929 cm^{-1} , and 3340 cm^{-1} which are attributed to the C-OH, C-H, and O-H bonds preset in lignocellulose.^[38] Distinctive lignin peaks are found on all the NSs at 1460 cm^{-1} , 1503 cm^{-1} and 1595 cm^{-1} .^[39] In addition, the hemicellulose and cellulose are confirmed by the peaks at 1054 cm^{-1} which is associated to the stretching vibrations of C-O-C.

Inside the nutshell structures, cellulose exists in the structure formed by lignin, while hemicellulose is tangled with cellulose, filling the gap between cellulose and lignin.^[40,41] This arrangement of these biopolymers plays a crucial role in their structural properties. Certain chemical treatments of the nutshells decrease the amount of lignin and disrupt the internal links among lignin, cellulose, and hemicellulose. That results in a greater amount of negative surface charges.^[37]

The zeta (ζ) potentials were analyzed for these four NSs depicted in **Table 1**. The results show a consistent range of ζ values, between -20 mV to -35 mV for these four NSs. The BET surface areas were analyzed before and after the acetone and ethanol solutions treatments. The results presented in **Table 1** indicates the marginal improvement of the surface areas because of this treatment.

Table 1: BET surface area and Zeta potential comparison of four nutshells

	WS	PS	FS	AS
BET Surface Area -Natural NS [m^2/g]	0.42	0.33	0.29	0.48
BET Surface Area - Treated NS [m^2/g]	0.62	0.55	0.49	0.76
Zeta potential [mV]	-32 mV	-20 mV	-35 mV	-28 mV

The water contact angle measurements **Figure 3 (b)** confirm that the natural nutshells (NNSs) are hydrophilic in nature regardless of any treatments. This indicates that water can easily enter their micro and nanochannels which is essential to the generation of streaming potential or streaming current. **Figure 3 (b)** also demonstrates the enhanced hydrophilicity of the nutshells after being treated with acetone and ethanol solutions and subsequently dried in a nitrogen environment. This treatment process reduces the nonproductive adsorption between lignin and cellulose proteins, and hence the hemicellulose and lignin components are partially weakened and removed.^[42] Furthermore, the execution of plasma treatment caused an incredibly hydrophilic surface which is confirmed by the water contact angle measurement (S-V1).

Therefore, more hydrophilic functional groups are exposed. Concurrently, densities showed small declines (**Figure-S 2**), means this treatment slightly enhanced porosity. It should be noted that this treatment didn't remove the lignin contents confirmed by the FT-IR spectra **Figure 3 (a)** and CLSM images **Figure 3 (d)**. To enhance the surface areas, additional treatments are required to remove the lignin and break the lignin and cellulose links. However, the elimination of lignin will cause a structural collapse that will compromise the stability of the device.^[43] Thus, the minor enhancement of the surface areas and porosity by these treatments ensures the long-term stability of the device. Out of these four NSs examined, the Almond Shell (AS) has the highest surface areas and porosity, while the pecan shell (PS) has the lowest surface areas and porosity, although the variations are quite small. Walnut shell (WS), on the other hand, demonstrates a well-balanced mix of surface areas, porosity, zeta potentials, and superior mechanical stability.^[44] Therefore, this study focuses on the functionally graded WS structure for most analyses.

Figure 3 (c) shows how color perception changes while exposed to the different treatments of WS. After being freeze-dried for 12 h, the color of the WS samples transforms from a dark orange tone to a pale orange.

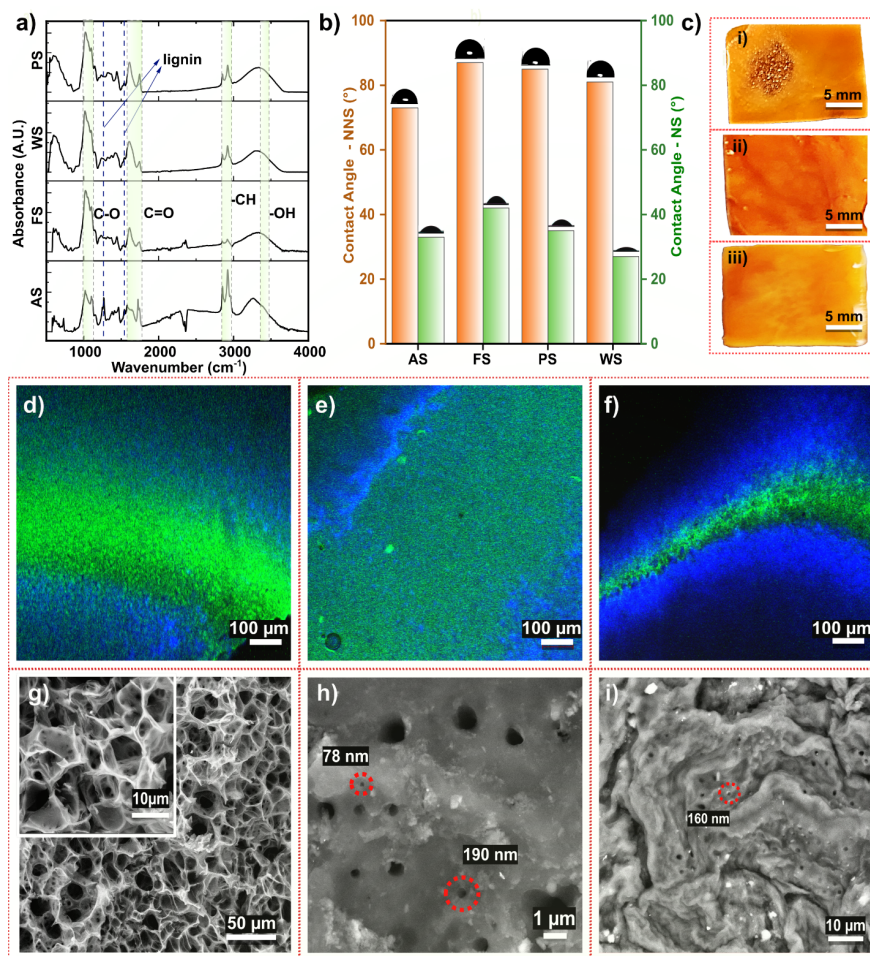


Figure 3: a) FT-IR spectra of the four NSs. b) Water contact angle of natural nut shells (NNS) and treated nut shells (NSs). c) Photograph of i) natural WS, ii) treated WS, and iii) nano-engineered WS-H⁺. Confocal Laser Scanning Microscopy (CLSM) of the d) untreated natural walnut shell (NWS), e) treated WS and f) WS-H⁺ indicating the lignin reductions (color changes from green to blue). SEM image of the g) porous, thin layer of inner shell surface of WS-H⁺, h) nanostructured outer shell surface of WS-H⁺ indicating the random pore diameter of 78 nm and 190 nm, i) WS-H⁺ after dipping in alkaline reservoir (pH 12.5) for 8 h with a random pore diameter of 160 nm.

The CLSM images of **Figure 3 (d, e, f)** confirms the variations in lignin contents in WS. The lignin (green) tends to disappear after undergoing the chemical treatments, and more cellulose (blue) gets exposed, which indicates the partial delignification of the WS. SEM images of WS-H⁺, shown in **Figure 3 (h)** confirms the enhanced number of nanopores after the nanoengineering of the WS. A prominently porous layer on the interior surface was also observed in **Figure 3 (g)**. **Figure 3 (i)** confirms the structural changes after dipping into the alkaline reservoir for 8 h, whereas the nanopores sustained.

Electricity generation and performance analyses

Herein, water droplet evaporation-based hydrovoltaic electricity generation has been investigated utilizing the nutshells. A sandwich structure of graphite-nutshell-graphite (G-NS-G) was utilized for the Open Circuit Voltage (V_{oc}), Short Circuit Current (I_{sc}), and Short Circuit Current density (J_{sc}) analyses. The typical

porous NS structure, as schematically illustrated in **Figure 4 (a)**, facilitates the water flow through the micro/nanochannels with multiple functional groups. When the DI water contacts this porous structure with abundant hydrophilic functional groups, water droplets are adsorbed and transferred through the micro/nanochannels under capillary action. At the same time, this abundant oxygenated functional group of the NS surface interacts with water and generates negative surface charges. Water is freely transferred throughout these channels under capillary actions and the continual evaporation helps to circulate the water in the direction of water evaporation. The transportation duration of water from the bottom surface to the top surface is different among these four NS, which is depicted in **Figure 4 (b)**. A very porous feature of AS along its surface and cross sections, confirmed by **Figure-S 3 (a)** causes the faster movement of water compared to other NSs.

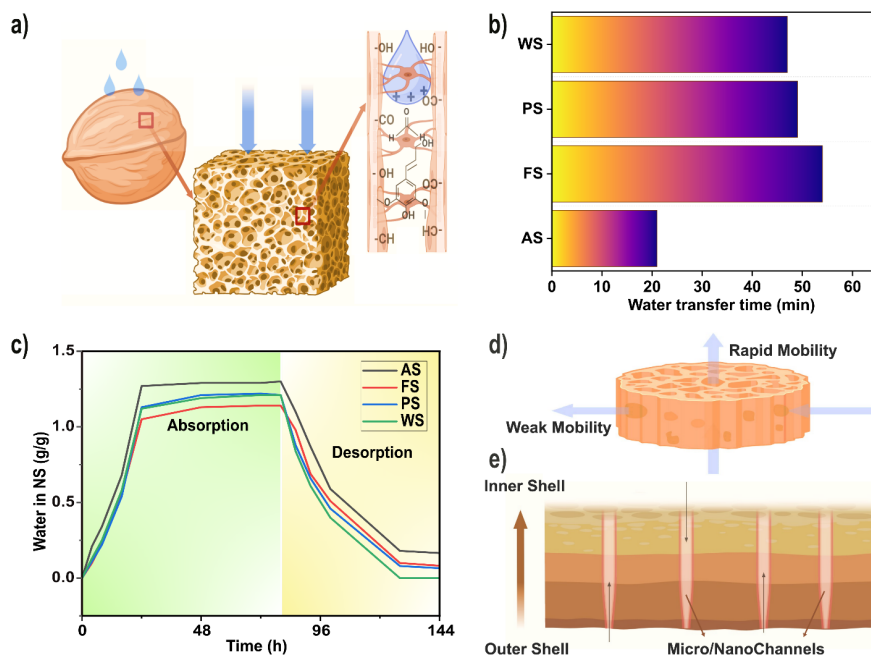


Figure 4: a) Illustration of the nutshell structure and movement of water droplet inside. b) Comparison of water transfer time from outer shell surface to inner shell surface of four NSs (thickness 1.6 mm); c) Evaluation of Water absorption and desorption kinetics of AS, FS, PS, WS at varying time intervals. d) Sketch of water transportation along cross-sectional and surface regions of WS, emphasizing higher mobility in surface-driven transport. g) Illustration of outer WS with a dense structure and inner WS with enhanced porosity, making convergent-divergent channels.

To evaluate the ability of the NSs to absorb and release water, each of the NS was immersed in DI water independently for a couple of days, and the resulting weight was periodically measured. Subsequently, the wet NS samples were subject to the ambient atmosphere ($T = 25\text{ }^{\circ}\text{C}$ and 30% Relative humidity) to evaluate the desorption of water because of the spontaneous evaporation. Multiple samples ($n=8$) were examined to validate the result. **Figure 4 (c)** demonstrates the capacity to absorb and release DI water over different durations. As anticipated, AS has the greatest capacity for absorption because of its exceptionally porous structure and lowest desorption rate due to its abundant vascular bundle,^[45] causing it to retain water for a longer duration. In contrast, WS desorbs the water quicker than other NS. This might be attributed to the higher concentration of hydrophobic lignin contents in WS, as presented in **Table-S 1**. The lignin and cellulose contain hydrophilic hydroxyl (-OH), carboxyl (-COOH) and carbonyl (C=O) functional groups and the aromatic hydrophobic functional groups.^[46] It has been proven that the balanced combination of hydrophilic and hydrophobic framework leads to enhanced evaporation rate.^[47,48] The cross-section of the

NSs was also experimented with for the water flow. Except for AS, all other NS exhibits reduced water mobility along the dense cross-section compared to the surface, as schematically illustrated in **Figure 4 (d)**. The outer shell surface seems denser than the inner shell surface, as schematically illustrated in **Figure 4 (e)**. Therefore, the time duration of water transport differs between the exterior and interior surfaces.

When each of the nutshells (NSs) is immersed in a small 1 ml droplet of deionized (DI) water, the bottom surface becomes saturated, inducing capillary flow to initiate and gradually spread the DI water to the top surface. This process can be accelerated by placing another tiny 0.3 ml DI water droplet on its upper surface. Capillary actions drive the bottom water to transfer upwards, while gravity helps the top water flow downwards. The phenomenon enabled by capillary forces and the directed gravitational flow of water via micro/nanochannels is attributed to the flow of water without using pumps. Subsequently, the whole porous structure transforms from a dry to a completely wet state, and water starts to evaporate naturally from the wet NS surfaces, as illustrated in **Figure 5 (a)**. Under identical experimental conditions, open circuit voltage (V_{oc}) and short circuit current density (J_{sc}) are recorded after the NSs are stabilized for 40 minutes at ambient conditions with 25% relative humidity (RH) and 25°C, for the G-NS-G structure containing AS, FS, PS, WS as illustrated in

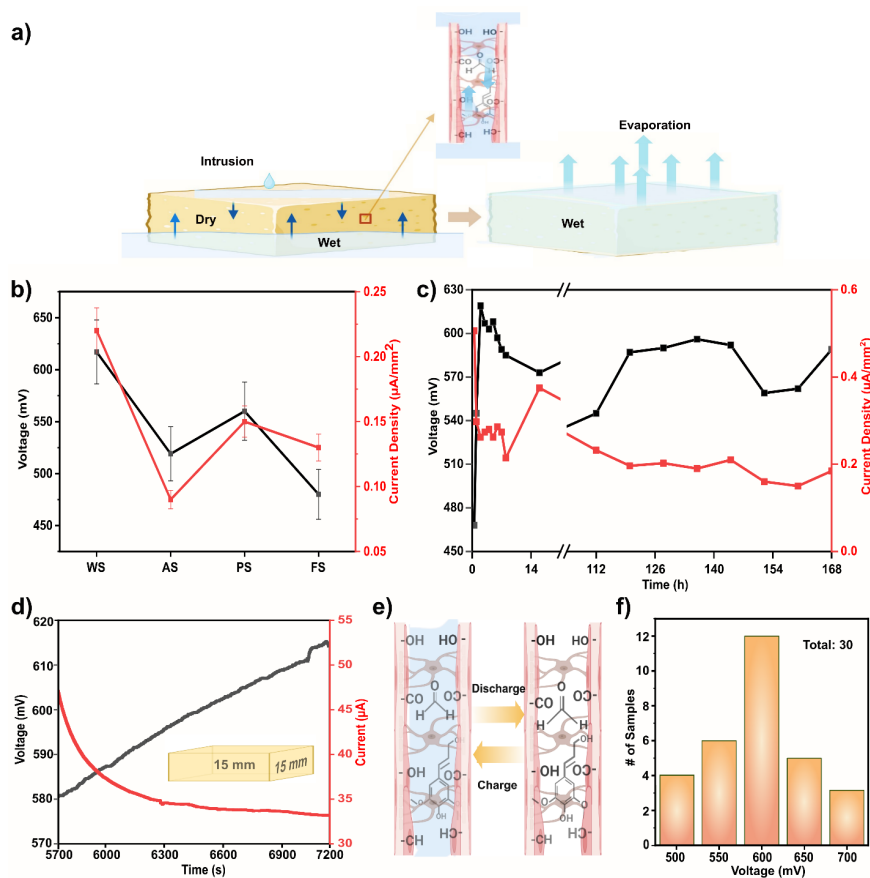


Figure 5: a) Schematic illustration of water intake mechanism of dry NS and evaporation on the wet NS structure, Inset showing transportation of water via natural evaporation and gravity through the Micro/Nanochannels. b) Open Circuit Voltage (V_{oc}) and Short Circuit Current density (J_{sc}) of four NSs. c) Long term reliability analyses of the WS-WEG for 1 week d) Typical V_{oc} and I_{sc} vs time for WS. e) Dry and wet WS as discharged and charged stage. f) Histogram of the V_{oc} for 30 WS-WEG samples.

The resulting G-NS-G structure exhibits an open circuit voltage (V_{oc}) above 500 mV and a short circuit

current density (J_{sc}) of over $0.1 \mu\text{A}/\text{mm}^2$ with a small amount of 1 ml drop DI water. The maximum current density (J_{sc}) was achieved by the swift transportation of electrons along the complete electrical circuit. The streaming potential, explained later in the mechanism section, shows the positive polarity towards the flow directions of the DI water. Therefore, only the positive polarity is considered throughout this study. The V_{oc} and I_{sc} show stable performance for a couple of hours because of the constant evaporation of water into the air. The orientation of these micro/nano-channels is placed parallelly to the direction of gravity and capillary induced water flow.

Among these four NSs, the WS displayed the most efficient J_{sc} , exceeding $0.20 \mu\text{A}/\text{mm}^2$, and V_{oc} , surpassing 600 mV. Multiple factors influence the output V_{oc} and J_{sc} of these four NSs. Distribution of the micro/nanochannels on the shell structure, porosity and their surface charge are the key parameters that affect the output V_{oc} and J_{sc} . Larger channel diameter, as seen in AS, shows low performance compared to WS, which can be explained by the equation of streaming potential. Because of the irregular channel structure and pore distributions, FS and PS also underperform compared with WS. Also, the asymmetrical-shaped narrow channels heighten hydrodynamic resistance. The highest evaporation rate of WS was observed in **Figure 4 (c)** also contributes to its superior electric performance.

WS exhibits superior uniformity, compact, and consistent channel structures among these four NSs, portrayed by large, interconnected 3D -puzzle cell, facilitating more efficient fluid flow than others.^[28,30,31] This simple G-WS-G device can generate a stable V_{oc} of 612 mV and J_{sc} of $0.15 \mu\text{A}/\text{mm}^2$ for a long duration. It consistently maintained an open circuit voltage above 550 mV and short circuit current above $17 \mu\text{A}$ (with 12 mm X 12 mm) for over a week without any substantial fluctuations, as seen in **Figure 5 (c)**. This signifies the long-term stability of the nutshell-based WEG devices. Replenishing the DI water every few hours at 0.3 ml/h maintained the evaporation process under 25% humidity and 25°C with full surface exposure. Because of the continuous evaporation of water, three layers are created on the shell structure: wet, dry, and partially wet. The partially wet regions present the highest contribution of streaming voltage.^[49]

Figure 5 (d) demonstrates the progressive rise in V_{oc} caused by the ongoing evaporation of DI water through the micro/nanochannels. The slower mobility of DI water leads to a prolonged duration for reaching the maximum voltage. A faster achievement of the stable state was feasible because of the simultaneous actions of gravity and capillary action. The V_{oc} reaches its maximum level while the specific saturation level is reached, and it remains constant. I_s decays because of the emission and readjustment of electrons and reaches a stable condition after a while. The NSs can continually harvest energy for a long time under wet conditions, however, the entirely dry NS doesn't have the capability of generating energy. Therefore, the wetted NS can be considered as charged whereas the fully arid NS can be considered as discharged, that is depicted in **Figure 5 (e)**. This nutshell-based WEG can be reused cyclically by drying the soaked NS and re-wetting it for energy harvesting.

Testing performed with platinum electrode (**Figure-S 6**) eliminates the possibilities of chemical reactions caused by the electrode contaminations. Output voltage and current values might vary slightly because of sample variations and measurement conditions. A total of 30 independent samples were inspected to confirm the reliability of the WS-WEG device (**Figure 5 (f)**). The findings signify that most samples demonstrated the revealed V_{oc} in the range of 580 mV to 620 mV.

Influential Factors Exploration on Device Performance

Multiple factors can influence the functionality of these WS-WEG devices during actual usage. Hence, a systematic investigation was carried out on several aspects, including relative humidity, temperature, different concentrations of NaCl solutions, heights of the shell structure, and polarity shifting of the device. The WS-WEG device was observed by placing it on different levels of water heights. It is observed in **Figure 6 (a)** that a partially submerged device, one end is exposed to air, sustains a consistent voltage due to water evaporation and the streaming potential effect. However, once the device becomes completely immersed, voltage reduces due to the inhibition of water evaporation, the major mechanism for electrical production.

The water evaporation rate decreased across the micro/nanochannels for the fully submerged device since the channels of the fully submerged device were partially impeded. Capillary flow along the channels is less prominent in fully submerged devices. Therefore, these devices show lower voltage compared with the partially submerged ones. Upon removal from the water reservoir, the device maintained in generating a low amount of voltage for a limited duration due to the evaporation of residual water content until it was completely dried.

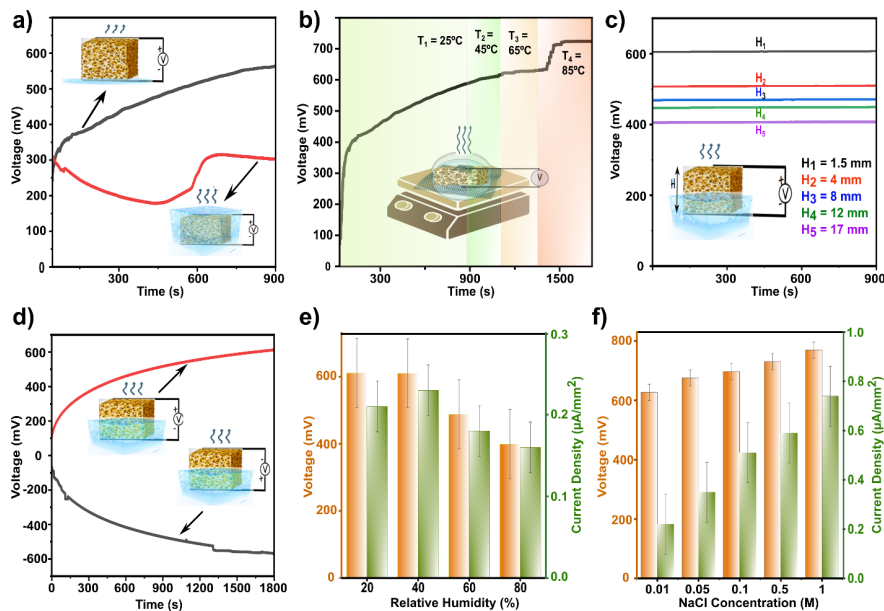


Figure 6: a) Exploration of the submerged level of water. b) Effect of heating the WS-WEG device. c) Evaluation of different heights of the WS. d) Voltage vs time with changing polarity. e) Effect of relative humidity level on V_{oc} and J_{sc} . f) Effect of NaCl concentration on V_{oc} and J_{sc} .

The temperature of the water reservoir was increased from 25°C to 85°C gradually to study the effects of the temperature, which is depicted in **Figure 6 (b)**. The results show that the V_{oc} gradually increases up to the voltage of 720 mV after a certain time while the temperature reaches 85°C . This can be attributed to the combined effects of the enhanced movement of water molecules, elevated evaporation rate, and thermoelectric effects.^[50] In addition, five different heights of the shell structure were examined to see the thickness effects on the V_{oc} . Since the thickness of the WS was under 2 mm, the cross-sectional configurations were considered for the elevated heights experiments. The density along the cross-section is comparatively higher, confirmed by SEM (Figure-S 3); therefore, the slightly lower voltage was observed. The results in **Figure 6 (c)** confirm that altered heights have a substantial effect on the V_{oc} . Elevated heights enhance the variations of ion concentrations; however, the more restrictions on water flow along the elevated cross sections reduce the output voltage.

By swapping the positive and negative electrodes on the multimeter, the polarity and magnitude of the open circuit voltage were compared. The results of **Figure 6 (d)** reveal that changing the polarity has no major impact on the voltage; the polarity changes only caused by the flipping. The effect of the humidity on the device performance was evaluated systematically. The results shown in **Figure 6 (e)** indicate the lower performance in extremely humid environments. This is due to the reduced evaporation rate in humid environments. While evaluating the effects of different concentrations of NaCl, the open circuit voltage seems to be higher at higher concentrations of NaCl, which is represented in **Figure 6 (f)**. Compared to water, NaCl leads to an enhanced voltage and current density of 703 mV and $0.78\ \mu\text{W}/\text{mm}^2$ respectively. Theoretically, enhanced concentrations of ions lead to a decrease in streaming potentials because of the

reduced size of the double layer.^[19] In this case, however, enhanced open circuit voltage are caused by the continuous evaporations of water. The higher solubility of NaCl and elevated migration rate of Na⁺ ions associated with WS micro/nanochannels facilitate the higher concentration gradients in the ionic pathway.^[51] The output voltage is, consequently, therefore, boosted by the enhanced level of ions in the solutions.

Performance enhancement and power density analyses

The acid-treated samples (WS-H⁺) were immersed in the reservoir of neutral water and alkaline solutions separately as illustrated in **Figure 7 (a)**. WS-H⁺ experiences a partial reduction of lignin and exposure of cellulose as observed in CLSM (**Figure 3 (f)**) and FT-IR spectra (**Figure 7 (b)**). As a result of this treatment additional nanochannels are created, as confirmed by the SEM (**Figure 3 (h)**), which can be referred to as nano-engineered WS-H⁺. C-O-C asymmetric stretching at 1160 cm⁻¹, C-H bending at 1360 cm⁻¹ and C-O-C stretching at 1105 cm⁻¹ confirms the presence of cellulose and C=O at 1040 cm⁻¹ confirms the stretching vibration of cellulose and hemicellulose^[52] which are prominent in the nano-engineered WS-H⁺ samples as confirmed by **Figure 7 (b)**.

Upon acid treatments the WS-H⁺ samples were protonated and the signals at 1738 cm⁻¹ disappeared after being placed on alkaline reservoir for 8 h as shown in **Figure-S 9**. The thermal gravimetric analyses at **Figure 7 (c)** demonstrates that the thermal stability of the natural walnut shell (NWS) is more than the treated WS and WS-H⁺. This is due to the reduction of lignin contents after the chemical treatments since lignin has higher thermal stability because of its complex heterogeneous structure.^[53]

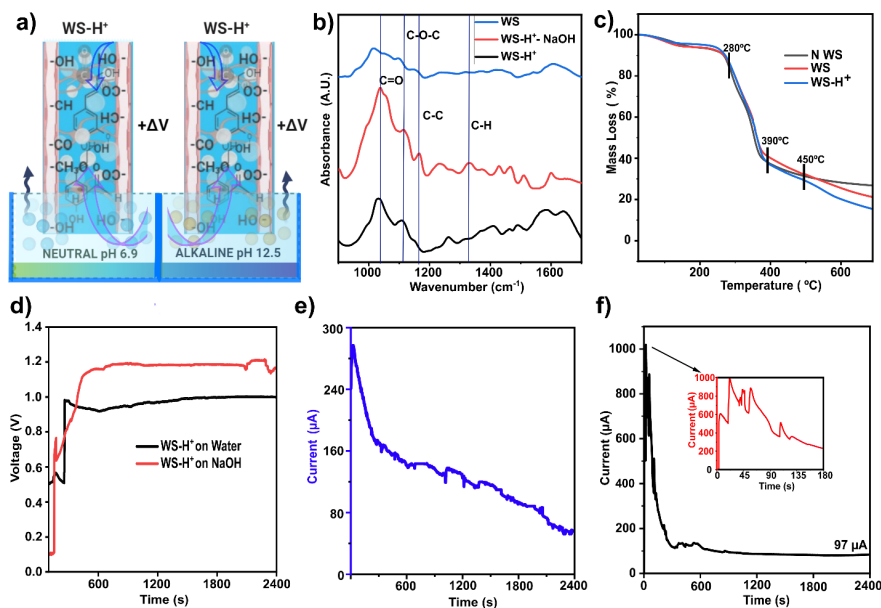


Figure 7: Illustration of WS-H⁺ WEG in reservoir of pH 6.9 and pH 12.5, creating a concentration gradient. b) FT-IR of WS, WS-H⁺ and WS-H⁺ on NaOH reservoir. c) TGA of Natural WS, Treated WS and WS-H⁺. d) V_{OC} enhancements of nano-engineered WS-H⁺. e) I_{SCC} of WS-H⁺ (16 mm X 18 mm) on DI water. f) I_{SCC} of WS-H⁺ (16 mm X 18 mm) on alkaline solution.

The WS-H⁺ samples were separately immersed into neutral reservoir of pH 6.9 as well as the alkaline reservoir with a pH of 12.5. Because of gravity, the top acid solutions travel toward the reservoir, whereas the solutions in the reservoir move upwards because of the action of capillary, causing the formation of concentration gradients as illustrated in **Figure 7 (a)**. **Figure 7 (d)** confirms the V_{oc} of 960 mV and **Figure 7 (e)** confirms the maximum I_{sc} of 288 μA when the sample was submerged in neutral solutions.

Figure 7 (d) also confirms the V_{oc} of 1.21 V when WS- H^+ was immersed in a solution with a pH of 12.5 and the I_{sc} reaches its maximum value of 1 mA as seen in **Figure 7 (f)**. The difference in pH levels between the WS- H^+ surface and the reservoir break apart the surface functional groups unevenly, leading to the enhanced output voltage and current. On top of that, these strong acid treatments enhance the surface area and surface charge.^[54,55] When the WS- H^+ is placed on the alkaline reservoir, gravity causes the H^+ ions to travel across the channel and fall into the reservoir underneath. Consequently, the H^+ ions react spontaneously with OH^- ions following the equation of $H^+ + OH^- = H_2O$ resulting in depletion of H^+ ions. Therefore, continuous migration of H^+ occurs in this acid-base reaction process. Furthermore, capillary-assisted upward movement of the OH^- ions and gravity-assisted downward migration of H^+ ions would result in the formation of a concentration gradient. The non-uniform distribution of a strong acid over the alkaline storage region would lead to an increase in both output voltage and current, as presented in the **Figure 7 (d, f)**. A potential difference is also created between the two electrodes because of the continuous movements of the H^+ and OH^- ions. Thus, the WS- H^+ devices achieved a revolutionary open circuit voltage of 1.21 V and a maximum short circuit current of 1 mA because of the combined influence of acid-base chemical processes, concentration gradients, streaming, and evaporation potentials compared with the original (WS-WEG) physically driven V_{oc} of 620 mV. This substantial contribution from the chemical reactions and concentration gradients were overlooked in the previous evaporation-driven WEG devices.^[16,18,56] The porous nutshells can also be considered as a separation membrane between the acid and base solutions. To sustain the reactions and concentration gradients the concentrated acid solutions were introduced on the top surface of the WS- H^+ at a rate of 0.1 ml/h. This remarkably efficient hydrovoltaic device demonstrates the highest current density of 347.2 $\mu A/cm^2$, representing a significant advancement.

Underlying operational mechanism of the device

The mechanism of this water-induced hydrovoltaic electricity generation is relatively complex. The basic mechanism involves ionization of the abundant functional groups on the channel wall of the nutshell surface upon water adsorption, leading to a negative surface charge. Meanwhile, the positive ions of the water will be absorbed on the negatively charged surface of the nutshell (NS), forming an electrical double layer (EDL),^[57] illustrated in **Figure 8 (b)**. The micro/nanochannels of the NS structures are considered as passive diffusion channels. In response to concentration gradients, passive diffusion of ions occurs across the shell structure without the need for outward energy input. The porous structures of the NS facilitate the movement of ions along their concentration gradient. Directional water flow inside the channels continues due to the water absorption on one side and evaporation on the other side. Because of the shearing effect of the water flow, the positive charged ions start to accumulate on the evaporation side of the NS. Only the positive ions can effectively traverse the negatively charged micro/nanochannels due to the strong electrostatic repulsion exerted by the negatively charged surface, hindering the penetration of negative ions.^[21,56] Due to the separation of charges, potential differences are created between the electrodes that drive electricity generation through the phenomenon of streaming potential. The flow direction determines the positive and negative polarity observed during measurements. An electric field is established as ions accumulate along the flow of water.^[21,58] The streaming potential increases linearly with the pressure difference that drives the water flow. The alteration in polarity inside the device is caused by the transpiration of water and the transport of ions via the micro/nano channels. As water drops on the top end, positively charged ions concentrate at the bottom electrode, generating positive polarity in the flow's direction. When water flow is exclusively dependent on the natural evaporation, the flow reverses from bottom to top, resulting in a polarity inversion that charges the top electrode positive. The streaming potential is contingent upon surface chemistry, ion transport, and flow dynamics within the micro/nano channels. Alterations in flow direction immediately affect the polarity of the generated voltage.

The phenomenon of streaming potential and streaming current can be explained by **Equation 1** and **Equation 2** and illustrated in **Figure 8 (a)**. Considering the cross-sectional area A as $(\pi\delta^2)/4$, the vertical pressure difference ΔH as $(4\gamma\cos\theta)/\delta$, the ultimate streaming potential and current can be expressed by **Equation 3** and **Equation 4**.^[59] The magnitude of the streaming potential depends on several factors,

including the properties of the liquid, the surface characteristics of the micro/nanochannel, and the flow rate of the liquid as seen **Equation 3**. Here micro/nanochannels of the NS that transport water are considered as a capillary tube. Water absorption within porous materials is contingent upon capillary forces, which can accelerate or deter water intrusion into the pores.

$$V_s = \frac{0r\Delta P\zeta}{\mu\sigma} \text{ Equation 1}$$

$$I_s = \frac{A_0r\Delta P\zeta}{\mu\Lambda} \text{ Equation 2}$$

$$V_s = \frac{4\epsilon_r\epsilon_0\cos}{\mu d} \text{ Equation 3}$$

$$I_s = \frac{d\epsilon_r\epsilon_0\cos}{\mu L} \text{ Equation 4}$$

$$R = \frac{8L\mu}{\pi r^4} \text{ Equation 5}$$

where L is capillary tube length, A is the cross-sectional area, ζ is the inner surface zeta potential, $\Delta\Pi$ external pressure difference, μ is dynamic viscosity, Q is the volumetric flow rate, r is the channel radius, ϵ_0 , ϵ_r , σ , γ , and μ are the dielectric constant, conductivity, specific tension, and viscosity of the DI water; R is the resistance of the water flow.

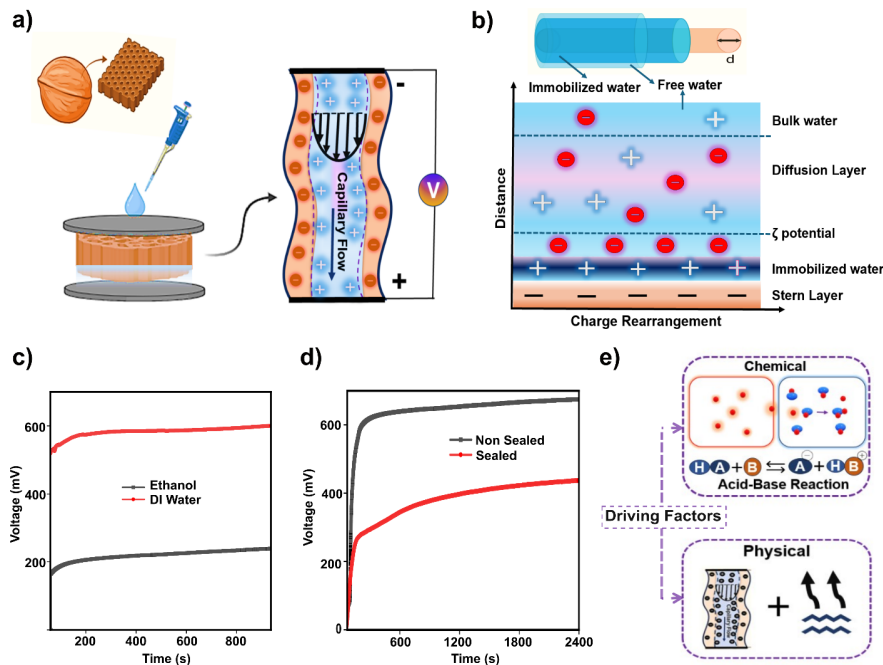


Figure 8: a) Schematic Illustration of ion transport in WS cell wall, and electricity generation via water transportation through the micro/nanochannels. b) Potential profile in the EDL at the NS/water interface. c) Comparison of V_{oc} on DI water and ethanol reservoirs. d) Effect of sealing on the output voltage. e) Illustration of the overall integrated underlined mechanisms of the high-performed WS- H^+ device.

It is evident from the equation that the streaming potential V_s can be very high by decreasing the channel diameter and decreasing the channel length can give higher streaming current I_s . The uneven diameter of the micro/nanochannels of the NS structures creates an elevated pressure difference ($\Delta\Pi$) that facilitates achieving superior V_s and I_s . However, very narrow channels introduce a high flow resistance which can be expressed by the Hagen–Poiseuille equation in **Equation 5**. A very high resistance may cancel the driving force from the capillary pressure, preventing flow through the channel and resulting in a substantially lower

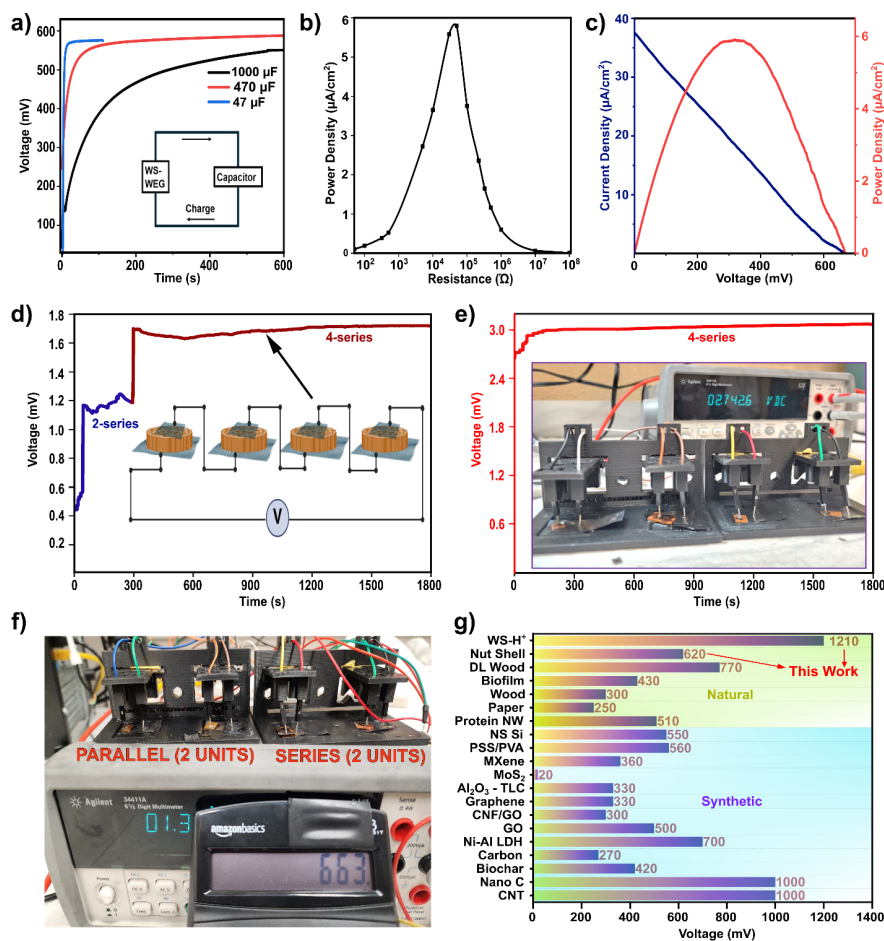
voltage and current output. Therefore, suitable channel dimensions are essential for achieving the optimised higher power output. Fine tuning of the device performance and channel dimension is required.

The effect of concentrations, debeye length, and EDL overlap is explained in the supplementary section, **Equation- S 1**. Water-evaporation-driven electricity generation has typically been recognized entirely as streaming potential.^[18] It is difficult to differentiate these two processes because of the absence of theoretical evidence and limited understanding of evaporation-induced capillary pressure and evaporation potentials. A very recent investigation focuses on illuminating the functions of evaporation potential and streaming potential in the generation of electricity.^[19] Based on that point of view, in this study, we explored the influence of evaporation potential through the utilization of two different approaches. Initially, we substituted the water with ethanol, which has lower zeta potential. The device maintains the ability to produce an open circuit voltage of 254 mV, depicted in **Figure 8 (c)**. A decrease from the initial 601 mV was observed with water as the medium. This implies that evaporation plays a partial role in the whole procedure, as clarified by the governing **Equation- S 2** for the potential of evaporation produced by ethanol. Additionally, sealing the device with an encloser leads to a reduction in voltage output from 617 mV to 412 mV after 10 minutes, as it successfully minimized evaporation, portrayed in **Figure 8 (d)**. These results emphasize the significant effect of both processes and signify that a substantial part of the voltage originates from the evaporation procedure.

This study aims to gather a full understanding of the reported events by inspecting the effects of different chemical treatments on ion transport and electricity generation. Whenever the WS-H⁺ samples were independently subjected to DI water and OH⁻solutions, the chemical reactions took place, which enhanced the output power. When H⁺ ions from the WS-H⁺ approached to OH⁻ ions of the solution, they interacted spontaneously as per the equation $H^+ + OH^- = H_2O$. Therefore, continuous movement and migration of H⁺ ions occur in the acid-base process. As long as the top and bottom surface of the WS has concentration variations (different functional groups), the V_{oc} and I_{sc} show elevated values. The differential ion flow causes an elevation in both open circuit voltage and short circuit current, which is mostly due to chemical reactions and partly due to underlying physical phenomena, as illustrated in **Figure 8 (e)**. To evaluate the effect of acid-base reactions, an additional experiment was performed by soaking regular paper in acid and placing it in an alkaline reservoir. The results revealed a substantial voltage, as seen in **Figure-S 7**.

Power density analyses and scalability for practical applications

These WS-WEG devices can charge commercial capacitors of 47 μ F, 470 μ F, and 1000 μ F, reaching the stable voltage of 615 mV without any secondary rectifier. **Figure 9 (a)** shows the required time to reach the peak voltage by these three capacitors is 15 s, 110 s which is very fast compared with the existing WEG devices [43], [60], [61]. **Figure 9 (b)** shows the power density of the WS-WEG device with the varied resistance from $10^1 \Omega$ to $10^8 \Omega$. The highest power density, 5.90 μ W/cm², of this WS-WEG device, was observed with the external load value of this WS-WEG device's current-voltage (I-V) characteristics were assessed. The **Figure 9 (c)** exhibits a linear reduction in voltage while applying current. Despite the application of a negative current, it is shown as positive for the purpose of simplicity. The highest power density was consistently measured as 5.96 μ W/cm². Scalability is essential for the practical use of any devices. Therefore, multiple devices were connected in series and parallel to justify their performance. **Figure 9 (d)** illustrates the V_{oc} of 1.77 V while connecting four WS-WEG units in series and **Figure 9 (e)** shows the V_{oc} of 3.18 V while connecting four WS-H⁺-WEG units in series. Therefore, two WS-H⁺-WEG units connected in series and two WS-H⁺-WEG units in parallel were able to power an LCD-screened calculator without the aid of any external boosters or rectifiers, as shown in **Figure 9 (f)** and S-V2. **Figure 9 (g)** depicts that these simple and innovative WS-WEG and WS-H⁺-WEG devices show outstanding performance compared with similar evaporation-driven WEG devices, which are based on conventional organic and inorganic materials.



Conclusion

Evaporation-driven WEG devices have gained significant attention since water is highly available and can easily evaporate. Several studies utilizing inorganic nanomaterials tend to overshadow the utilization of easily accessible organic materials. This study presents an innovative electricity generation method that employs the nutshell (NS) structures by leveraging the process of streaming potential and water evaporations. This revolutionary bio-based technology is presented for the first time and utilizes inherent hierarchical porous structures of NSs for efficient ion transfer, enabling the WEG device to function sustainably with minimum water intake. Amongst the four NSs investigated, walnut shell (WS) exhibits superior performance due to its uniform pore distributions, surface charge, and efficient water uptake and release capabilities. Other NSs are also a promising source of WEG that need further attention. A consistent electric output over 550 mV for a duration of one week, demonstrates the long-term stability of the WS-WEG. Moreover, this WS-WEG functional device's incredible power density (5.96 $\mu\text{W}/\text{cm}^2$) indicates its enormous potential for practical use. A notable enhancement of the voltage and current density is observed by utilizing nanoengineering techniques that enhance the number of nanopores. Furthermore, placing the nano-engineered WS-H⁺ into an alkaline reservoir shows a significant rise in voltage to 1.21 V and a maximum current density of 347.2 $\mu\text{A}/\text{cm}^2$. This enhancement could be attributed to the combined synergetic impacts of physical and chemical mechanisms. By connecting two units in series and two units in parallel, this WS-H⁺ can power a calculator without the aid of any rectifiers, indicating the potentiality of this WEG device as a sustainable power source for compact electronics. In summary, this work not only develops the comprehension of nutshell-

based WEG but also offers a feasible, low-cost, sustainable energy source utilizing agro-industrial waste to power electronic devices.

Experimental Details

Materials Unprocessed, dried, raw nuts with their shells intact (Almond, Filbert/Hazelnut, Pecan, Walnut) were procured directly from YuPik, Montreal, QC, Canada. The nuts were originally grown in the USA. Ethanol (C₂H₆O), Acetone (C₃H₆O), Sodium hydroxide (NaOH), Potassium Hydroxide (KOH), Hydrochloric Acid (HCl), Sulfuric Acid (H₂SO₄), and Nitric Acid (HNO₃) were obtained from Fisher Scientific.

Sample Preparation

The nutshells were cracked by a nutcracker and the kernels were isolated from the shell. The shells were then segmented by Epilog Fusion M2 laser cutter using CO₂ laser and subsequently sanded to a required uniform dimension. Sanding the cross-sectional areas also helps to remove the laser-induced localized burned regions. The inner and outer surface of the shells were also sanded partially to mitigate uneven surface of the shell morphology. **The samples obtain a uniform form, making them suitable for application into numerous practical devices.** Samples were then cleaned with ultrapure water. Nutshell samples were immersed in a solution consisting of 40% (v/v) acetone, 30% (v/v) ethanol, and 30% (v/v) deionized (DI) water. The mixture was heated at 70 °C for 20 minutes to break the lignin and hemicellulose network. Samples were rinsed thoroughly with ultra-pure water to eliminate the residues. Following the treatments the samples were dried in a tube furnace at 100 °C for 1 h under a constant flow of nitrogen gas. After being dried in the ambient environment for 24 h, the samples are marked as Almond Shell - AS, Filbert Shell - FS, Pecan Shell - PS, and Walnut Shell - WS. To enhance the hydrophilicity, a few of the samples were further plasma cleaned for 8 minutes.

WS-H⁺ preparation

To enhance the electrical power generation from the WS-WEG, the WS was further treated in acid solutions containing Hydrochloric Acid (3 M) 40% vol, Sulfuric Acid (3 M) 30% vol, and Nitric Acid (3M) 30% vol. After freeze drying at -12 °C for 12 h, and cleaning with DI water a nano-engineered WS was formed, which was designated as WS-H⁺. The WS-H⁺ samples were subsequently put independently on reservoirs holding neutral solutions (pH 6.9) and alkaline solutions (pH 12.5) with NaOH of 80% (v/v) and NaCl of 20% (v/v).

Characterization

The morphology and architectural characteristics of the NSs were investigated using environmental scanning electron microscopy (ESEM) (Quanta FEG 250 ESEM, FEI, USA). To avoid the coating on the sample surface and thus retain the surface's integrity, this ESEM was operated in low vacuum mode. ESEM was used to thoroughly examine the inner and exterior surfaces and cross section of all NS samples at different magnifications. The chemical functionalities of the nutshell samples were examined by a Bruker Tensor 27 FTIR spectrometer (PIKE Technologies, USA) equipped with an attenuated total reflectance (ATR). With multiple consecutive scans, the infrared spectra were gained in the wavenumber range of 4000 - 400 cm⁻¹ at room temperature. A Confocal laser scanning microscopy - CLSM (Zeiss LSM 510 confocal microscope) imaging was carried out to examine the distribution of lignin, cellulose, and hemicellulose within the cross-section of the WS. Cross sections of the WS samples were sanded to a thickness of less than 50 μm before the analyses. Lignin can be directly determined in the microscope since it has the property of autofluorescence.^[77] To reveal the cellulose and hemicellulose, the samples were treated with Calcofluor White Stain (Sigma-Aldrich, Canada) and a 1 M KOH aqueous solution (Sigma-Aldrich, Canada) for a duration of 5 minutes. Afterward, the samples were stimulated with a laser emitting light at a wavelength of 488 nm (detection range of 470 – 630 nm) to visualize lignin and at a wavelength of 405 nm (detection range of 425 – 450 nm) to detect cellulose and hemicellulose. Zeta potentials of the nutshells were measured by using a Dynamic Light Scattering (DLS) - (Malvern Zetasizer Nano ZS, UK). Prior to the zeta potential analysis, the

nutshells were ball-milled at 550 rpm for 30 minutes using a (Retsch planetary ball mill PM 200 with agate and stainless-steel grinding jars) ball mill with 4 stainless steel (SS) balls. A 5% v/v suspension of each sample was prepared in Milli-Q water. The zeta potential of each nutshell sample was then determined three times for better reliability. The Optical Contact Angle (OCA 35) instrument measured the water contact angle of the surfaces. The surface area of each of the NSs was analyzed by multipoint BET methods (Gemini VII 2390A, Micromeritics, USA). Samples were degassed at 80 °C for 10 h in nitrogen environment prior to the SA analyses. Thermal Gravimetric Analyses (Q500, TA instruments, USA) were conducted for the walnut shell samples in a nitrogen environment within the temperature range from RT to 700 °C.

Electricity generation setup

For the electrical performance evaluations, high purity, flexible graphite sheets with a thickness of 0.05 mm, a density of 1-1.5 g/cm³, and carbon content of 99.9% were used as electrode, making a sandwich structure of graphite-nutshell-graphite (G-NS-G). The high-purity graphite sheet was selected because of its non-polarization property and cost effectiveness. On top of that, these thin, flexible graphite sheets can be adhered to the surface of the NSs when wet. The top graphite electrode covers less than 20% of the entire top surface, allowing the available free surface for effective water evaporation. A unique 3D printed setup, illustrated in **Figure-S 4**, had been constructed for the reliable electric connection. A small drop of Deionized (DI) water (1 ml) was used as water reservoir. The nutshell-based WEGs were connected to the multimeter (Agilent 34411A, Keysight, USA), SourceMeter (model B2901BL, Keysight, USA) and Potentiostat / Galvanostat (Interface 1010 E, Gamry, USA) to record the output voltage and current.

Supporting Information :

Supporting Information is available from the Wiley Online Library.

Acknowledgements

The authors like to acknowledge the Waterloo Advanced Technology Laboratory (WATLAB), Analytical Facilities and the Wettig Research Group at the University of Waterloo, Waterloo, Canada, and Biointerfaces Institute at the McMaster University, Hamilton, Canada for their valuable support in carrying out few of the experiments.

References:

- [1] T. Li and P. S. Lee, “Piezoelectric Energy Harvesting Technology: From Materials, Structures, to Applications,” *Small Structures* , vol. 3, no. 3. John Wiley and Sons Inc, Mar. 01, 2022. doi: 10.1002/ssstr.202100128.
- [2] D. W. Kim, J. H. Lee, J. K. Kim, and U. Jeong, “Material aspects of triboelectric energy generation and sensors,” *NPG Asia Materials* , vol. 12, no. 1. Nature Research, Dec. 01, 2020. doi: 10.1038/s41427-019-0176-0. [3] A. G. Rösch *et al.* , “Fully printed origami thermoelectric generators for energy-harvesting,” *npj Flexible Electronics* , vol. 5, no. 1, Dec. 2021, doi: 10.1038/s41528-020-00098-1. [4] Y. Xu, T. Xu, J. Wang, W. Liu, and J. Wang, “Microvessel-Assisted Environmental Thermal Energy Extraction Enabling 24-Hour Continuous Interfacial Vapor Generation,” *ChemSusChem* , vol. 13, no. 24, pp. 6635–6642, Dec. 2020, doi: 10.1002/cssc.202002238. [5] E. A. Grubert, “Water consumption from hydroelectricity in the United States,” *Adv Water Resour* , vol. 96, pp. 88–94, Oct. 2016, doi: 10.1016/j.advwatres.2016.07.004. [6] J. Zhang, X. Lei, B. Chen, and Y. Song, “Analysis of blue water footprint of hydropower considering allocation coefficients for multi-purpose reservoirs,” *Energy* , vol. 188, Dec. 2019, doi: 10.1016/j.energy.2019.116086. [7] Z. Zhang *et al.* , “Emerging hydrovoltaic technology,” *Nature Nanotechnology* , vol. 13, no. 12. Nature Publishing Group, pp. 1109–1119, Dec. 01, 2018. doi: 10.1038/s41565-018-0228-6. [8] J. Yin, J. Zhou, S. Fang, and W. Guo, “Hydrovoltaic Energy on the Way,” 2020. [9] X. Huangfu, Y. Guo, S. M. Mugo, and Q. Zhang, “Hydrovoltaic Nanogenerators for Self-Powered Sweat Electrolyte Analysis,” *Small* , vol. 19, no. 15, Apr. 2023, doi: 10.1002/sml.202207134. [10] S. Jiao *et al.* , “Graphene oxide as a versatile platform for emerging hydrovoltaic technology,” *Journal of Materials Chemistry A* , vol. 10, no. 36. Royal Society of

Chemistry, pp. 18451–18469, Jul. 25, 2022. doi: 10.1039/d2ta04830b. [11] J. Yin, X. Li, J. Yu, Z. Zhang, J. Zhou, and W. Guo, “Generating electricity by moving a droplet of ionic liquid along graphene,” *Nat Nanotechnol*, vol. 9, no. 5, pp. 378–383, 2014, doi: 10.1038/nnano.2014.56. [12] H. Zhong *et al.*, “Graphene based two dimensional hybrid nanogenerator for concurrently harvesting energy from sunlight and water flow,” *Carbon N Y*, vol. 105, pp. 199–204, Aug. 2016, doi: 10.1016/j.carbon.2016.04.030. [13] J. Li *et al.*, “Electricity generation from water droplets via capillary infiltrating,” *Nano Energy*, vol. 48, pp. 211–216, Jun. 2018, doi: 10.1016/j.nanoen.2018.02.061. [14] W. Fei, C. Shen, S. Zhang, H. Chen, L. Li, and W. Guo, “Waving potential at volt level by a pair of graphene sheets,” *Nano Energy*, vol. 60, pp. 656–660, Jun. 2019, doi: 10.1016/j.nanoen.2019.04.020. [15] J. Tan, J. Duan, Y. Zhao, B. He, and Q. Tang, “Generators to harvest ocean wave energy through electrokinetic principle,” *Nano Energy*, vol. 48, pp. 128–133, Jun. 2018, doi: 10.1016/j.nanoen.2018.03.032. [16] Q. Hu, Y. Ma, G. Ren, B. Zhang, and S. Zhou, “Water evaporation-induced electricity with *Geobacter sulfurreducens* biofilms,” 2022. [Online]. Available: <https://www.science.org> [17] X. Li, K. Zhang, A. Nilghaz, G. Chen, and J. Tian, “A green and sustainable water evaporation-induced electricity generator with woody biochar,” *Nano Energy*, vol. 112, Jul. 2023, doi: 10.1016/j.nanoen.2023.108491. [18] G. Xue *et al.*, “Water-evaporation-induced electricity with nanostructured carbon materials,” *Nat Nanotechnol*, vol. 12, no. 4, pp. 317–321, May 2017, doi: 10.1038/nnano.2016.300. [19] S. Fang, H. Lu, W. Chu, and W. Guo, “Mechanism of water-evaporation-induced electricity beyond streaming potential,” *Nano Research Energy*, vol. 3, no. 2, Jun. 2024, doi: 10.26599/NRE.2024.9120108. [20] J. Tan *et al.*, “Self-sustained electricity generator driven by the compatible integration of ambient moisture adsorption and evaporation,” *Nat Commun*, vol. 13, no. 1, Dec. 2022, doi: 10.1038/s41467-022-31221-7. [21] D. Xu, M. Yan, and Y. Xie, “Energy harvesting from water streaming at charged surface,” *Electrophoresis*, vol. 45, no. 3–4. John Wiley and Sons Inc, pp. 244–265, Feb. 01, 2024. doi: 10.1002/elps.202300102. [22] K. Xiao, L. Jiang, and M. Antonietti, “Ion Transport in Nanofluidic Devices for Energy Harvesting,” *Joule*, vol. 3, no. 10. Cell Press, pp. 2364–2380, Oct. 16, 2019. doi: 10.1016/j.joule.2019.09.005. [23] Y. Liu, Y. Zheng, T. Li, D. Wang, and F. Zhou, “Water-solid triboelectrification with self-repairable surfaces for water-flow energy harvesting,” *Nano Energy*, vol. 61, pp. 454–461, Jul. 2019, doi: 10.1016/j.nanoen.2019.05.007. [24] F. Galembeck, L. P. Santos, T. A. L. Burgo, and A. Galembeck, “The emerging chemistry of self-electrified water interfaces,” *Chemical Society Reviews*, vol. 53, no. 5. Royal Society of Chemistry, pp. 2578–2602, Feb. 02, 2024. doi: 10.1039/d3cs00763d. [25] Y. Gao *et al.*, “Gradient Free Nanoinjection of Fe₃O₄ into Wood for Enhanced Hydrovoltaic Energy Harvesting,” *ACS Sustain Chem Eng*, vol. 11, no. 30, pp. 11099–11109, Jul. 2023, doi: 10.1021/acssuschemeng.3c01649. [26] J. Garemark *et al.*, “Advancing Hydrovoltaic Energy Harvesting from Wood through Cell Wall Nanoengineering,” *Adv Funct Mater*, vol. 33, no. 4, Jan. 2023, doi: 10.1002/adfm.202208933. [27] X. Zhou *et al.*, “Harvesting Electricity from Water Evaporation through Microchannels of Natural Wood,” *ACS Appl Mater Interfaces*, vol. 12, no. 9, pp. 11232–11239, Mar. 2020, doi: 10.1021/acscami.9b23380. [28] J. Nicolás-Bermúdez *et al.*, “Characterization of the hierarchical architecture and micromechanical properties of walnut shell (*Juglans regia* L.),” *J Mech Behav Biomed Mater*, vol. 130, Jun. 2022, doi: 10.1016/j.jmbbm.2022.105190. [29] C. A. Toles, W. E. Marshall, and M. M. Johns, “Surface functional groups on acid-activated nutshell carbons,” 1999. [30] S. J. Antreich, J. C. Huss, N. Xiao, A. Singh, and N. Gierlinger, “The walnut shell network: 3D visualisation of symplastic and apoplastic transport routes in sclerenchyma tissue,” *Planta*, vol. 256, no. 3, Sep. 2022, doi: 10.1007/s00425-022-03960-w. [31] J. C. Huss *et al.*, “Topological Interlocking and Geometric Stiffening as Complementary Strategies for Strong Plant Shells,” *Advanced Materials*, vol. 32, no. 48, Dec. 2020, doi: 10.1002/adma.202004519. [32] S. J. Antreich *et al.*, “The Puzzle of the Walnut Shell: A Novel Cell Type with Interlocked Packing,” *Advanced Science*, vol. 6, no. 16, Aug. 2019, doi: 10.1002/advs.201900644. [33] N. Xiao *et al.*, “Twist and lock: Nutshell structures for high strength and energy absorption,” *R Soc Open Sci*, vol. 8, no. 8, Aug. 2021, doi: 10.1098/rsos.210399. [34] F. Brleković, K. Mužina, and S. Kurajica, “The Influence of Alkaline Pretreatment of Waste Nutshell for Use in Particulate Biocomposites,” *Journal of Composites Science*, vol. 8, no. 1, Jan. 2024, doi: 10.3390/jcs8010026. [35] X. Li, Y. Liu, J. Hao, and W. Wang, “Study of almond shell characteristics,” *Materials*, vol. 11, no. 9, Sep. 2018, doi: 10.3390/ma11091782. [36] R. Md Salim, J. Asik, and M. S. Sarjadi, “Chemical functional groups of extractives, cellulose and lignin extracted from native *Leucaena leucocephala* bark,” *Wood Sci Technol*, vol. 55, no. 2, pp. 295–313, Mar. 2021, doi: 10.1007/s00226-020-01258-2. [37] M.

Zhang *et al.* , “Lignocellulosic materials for energy storage devices,” *Ind Crops Prod* , vol. 203, Nov. 2023, doi: 10.1016/j.indcrop.2023.117174. [38] C. M. Popescu, M. C. Popescu, and C. Vasile, “Structural analysis of photodegraded lime wood by means of FT-IR and 2D IR correlation spectroscopy,” *Int J Biol Macromol* , vol. 48, no. 4, pp. 667–675, 2011, doi: 10.1016/j.ijbiomac.2011.02.009. [39] F. Kačík, J. Luptáková, P. Šmíra, A. Nasswettrová, D. Kačíková, and V. Vacek, “Chemical alterations of pine wood lignin during heat sterilization,” *Bioresources* , vol. 11, no. 2, pp. 3442–3452, May 2016, doi: 10.15376/biores.11.2.3442-3452. [40] Z. Shugang, W. Jing, W. Hongxia, Z. Zhihua, and L. Xibo, “Changes in Lignin Content and Activity of Related Enzymes in the Endocarp During the Walnut Shell Development Period,” *Hortic Plant J* , vol. 2, pp. 141–146, 2016, doi: 10.16420/j.issn.0513-353x.2015-0261. [41] J. Zhang, Y. S. Choi, C. G. Yoo, T. H. Kim, R. C. Brown, and B. H. Shanks, “Cellulose-hemicellulose and cellulose-lignin interactions during fast pyrolysis,” *ACS Sustain Chem Eng* , vol. 3, no. 2, pp. 293–301, Feb. 2015, doi: 10.1021/sc500664h. [42] W. Ying, Z. Shi, H. Yang, G. Xu, Z. Zheng, and J. Yang, “Effect of alkaline lignin modification on cellulase-lignin interactions and enzymatic saccharification yield,” *Biotechnol Biofuels* , vol. 11, no. 1, Aug. 2018, doi: 10.1186/s13068-018-1217-6. [43] J. Lin *et al.* , “All Wood-Based Water Evaporation-Induced Electricity Generator,” *Adv Funct Mater* , 2024, doi: 10.1002/adfm.202314231. [44] J. Nicolás-Bermúdez *et al.* , “Characterization of the hierarchical architecture and micromechanical properties of walnut shell (*Juglans regia* L.),” *J Mech Behav Biomed Mater* , vol. 130, Jun. 2022, doi: 10.1016/j.jmbbm.2022.105190. [45] S. R. *, G. C. , F. S. , C. A. C. , G. C. , G. L. , L. B. , A. S. , M. B. Aurora Modicaa *et al.* , “Solid state ¹³C-NMR methodology for the cellulose composition studies of the shells of *Prunus dulcis* and their derived cellulosic materials,” *Carbohydr Polym* , vol. 240, Jul. 2020, doi: 10.1016/j.carbpol.2020.116290. [46] M. Erfani Jazi *et al.* , “Structure, chemistry and physicochemistry of lignin for material functionalization,” *SN Applied Sciences* , vol. 1, no. 9. Springer Nature, Sep. 01, 2019. doi: 10.1007/s42452-019-1126-8. [47] R. Wan, C. Wang, X. Lei, G. Zhou, and H. Fang, “Enhancement of Water Evaporation on Solid Surfaces with Nanoscale Hydrophobic-Hydrophilic Patterns,” *Phys Rev Lett* , vol. 115, no. 19, Nov. 2015, doi: 10.1103/PhysRevLett.115.195901. [48] “S1385894723015693 (1)”. [49] S. Fang, H. Lu, W. Chu, and W. Guo, “Mechanism of water-evaporation-induced electricity beyond streaming potential,” *Nano Research Energy* , vol. 3, no. 2, Jun. 2024, doi: 10.26599/NRE.2024.9120108. [50] M. F. Sanad, A. E. Shalan, S. O. Abdellatif, E. S. A. Serea, M. S. Adly, and M. A. Ahsan, “Thermoelectric Energy Harvesters: A Review of Recent Developments in Materials and Devices for Different Potential Applications,” *Topics in Current Chemistry* , vol. 378, no. 6. Springer Science and Business Media Deutschland GmbH, Dec. 01, 2020. doi: 10.1007/s41061-020-00310-w. [51] C. Wang, S. Tang, B. Li, J. Fan, and J. Zhou, “Construction of hierarchical and porous cellulosic wood with high mechanical strength towards directional Evaporation-driven electrical generation,” *Chemical Engineering Journal* , vol. 455, Jan. 2023, doi: 10.1016/j.cej.2022.140568. [52] Y. Yang *et al.* , “Fourier-transform infrared spectroscopy analysis of the changes in chemical composition of wooden components in the ancient building of xichuan guild hall,” *For Prod J* , vol. 70, no. 4, pp. 448–452, 2020, doi: 10.13073/FPJ-D-20-00028. [53] B. A. Salazar-Cruz, M. Y. Chávez-Cinco, A. B. Morales-Cepeda, C. E. Ramos-Galván, and J. L. Rivera-Armenta, “Evaluation of Thermal Properties of Composites Prepared from Pistachio Shell Particles Treated Chemically and Polypropylene,” *Molecules* , vol. 27, no. 2, Jan. 2022, doi: 10.3390/molecules27020426. [54] H. Albatrni, H. Qiblawey, and M. J. Al-Marri, “Walnut shell based adsorbents: A review study on preparation, mechanism, and application,” *Journal of Water Process Engineering* , vol. 45. Elsevier Ltd, Feb. 01, 2022. doi: 10.1016/j.jwpe.2021.102527. [55] C. S. V. G. Esteves, E. Brännvall, S. Östlund, and O. Sevastyanova, “Evaluating the Potential to Modify Pulp and Paper Properties through Oxygen Delignification,” *ACS Omega* , vol. 5, no. 23, pp. 13703–13711, Jun. 2020, doi: 10.1021/acsomega.0c00869. [56] T. Tabrizizadeh, J. Wang, R. Kumar, S. Chaurasia, K. Stamplecoskie, and G. Liu, “Water-Evaporation-Induced Electric Generator Built from Carbonized Electrospun Polyacrylonitrile Nanofiber Mats,” *ACS Appl Mater Interfaces* , vol. 13, no. 43, pp. 50900–50910, Nov. 2021, doi: 10.1021/acsmi.1c13487. [57] S. J. Shin *et al.* , “On the importance of the electric double layer structure in aqueous electrocatalysis,” *Nat Commun* , vol. 13, no. 1, Dec. 2022, doi: 10.1038/s41467-021-27909-x. [58] T. G. Yun, J. Bae, A. Rothschild, and I. D. Kim, “Transpiration Driven Electrokinetic Power Generator,” *ACS Nano* , vol. 13, no. 11, pp. 12703–12709, Nov. 2019, doi: 10.1021/acsnano.9b04375. [59] P.-G. de Gennes, F. Brochard-Wyart, and D. Quéré, *Capillarity and Wetting Phenomena* . Springer New York, 2004. doi: 10.1007/978-0-387-21656-0. [60] C. Wang, S. Tang, B. Li, J. Fan, and J. Zhou, “Construction of hierarchical

and porous cellulosic wood with high mechanical strength towards directional Evaporation-driven electrical generation,” *Chemical Engineering Journal* , vol. 455, Jan. 2023, doi: 10.1016/j.cej.2022.140568. [61] H. Wang *et al.* , “Bilayer of polyelectrolyte films for spontaneous power generation in air up to an integrated 1,000 V output,” *Nat Nanotechnol* , vol. 16, no. 7, pp. 811–819, Jul. 2021, doi: 10.1038/s41565-021-00903-6. [62] X. Zhou *et al.* , “Harvesting Electricity from Water Evaporation through Microchannels of Natural Wood,” *ACS Appl Mater Interfaces* , vol. 12, no. 9, pp. 11232–11239, Mar. 2020, doi: 10.1021/acsami.9b23380. [63] X. Liu *et al.* , “Microbial biofilms for electricity generation from water evaporation and power to wearables,” *Nat Commun* , vol. 13, no. 1, Dec. 2022, doi: 10.1038/s41467-022-32105-6. [64] X. Li, K. Zhang, A. Nilghaz, G. Chen, and J. Tian, “A green and sustainable water evaporation-induced electricity generator with woody biochar,” *Nano Energy* , vol. 112, Jul. 2023, doi: 10.1016/j.nanoen.2023.108491. [65] Y. J. Ma, G. P. Ren, Y. R. Qiu, S. G. Zhou, and Q. C. Hu, “Electricity generation from *Geobacter sulfurreducens* biofilm and its sensing application,” *Zhongguo Kexue Jishu Kexue/Scientia Sinica Technologica* , vol. 52, no. 11, pp. 1669–1678, 2022, doi: 10.1360/SST-2022-0062. [66] J. Sun *et al.* , “Electricity generation from a Ni-Al layered double hydroxide-based flexible generator driven by natural water evaporation,” *Nano Energy* , vol. 57, pp. 269–278, Mar. 2019, doi: 10.1016/j.nanoen.2018.12.042. [67] Q. Liu *et al.* , “A Continuous Gradient Chemical Reduction Strategy of Graphene Oxide for Highly Efficient Evaporation-Driven Electricity Generation,” *Small Methods* , vol. 7, no. 9, Sep. 2023, doi: 10.1002/smt.202300304. [68] C. Li, Z. Tian, L. Liang, S. Yin, and P. K. Shen, “Electricity Generation from Capillary-Driven Ionic Solution Flow in a Three-Dimensional Graphene Membrane,” *ACS Appl Mater Interfaces* , vol. 11, no. 5, pp. 4922–4929, Feb. 2019, doi: 10.1021/acsami.8b16529. [69] D. He *et al.* , “Electricity generation from phase-engineered flexible MoS₂ nanosheets under moisture,” *Nano Energy* , vol. 81, Mar. 2021, doi: 10.1016/j.nanoen.2020.105630. [70] P. Xiao *et al.* , “Exploring interface confined water flow and evaporation enables solar-thermal-electro integration towards clean water and electricity harvest via asymmetric functionalization strategy,” *Nano Energy* , vol. 68, Feb. 2020, doi: 10.1016/j.nanoen.2019.104385. [71] X. Zhang, Y. Wang, X. Zhang, C. W. Lou, J. H. Lin, and T. T. Li, “Preparation and study of bark-like MXene based high output power hydroelectric generator,” *Chemical Engineering Journal* , vol. 465, Jun. 2023, doi: 10.1016/j.cej.2023.142582. [72] T. Xu *et al.* , “Electric Power Generation through the Direct Interaction of Pristine Graphene-Oxide with Water Molecules,” *Small* , vol. 14, no. 14, Apr. 2018, doi: 10.1002/sml.201704473. [73] X. Liu *et al.* , “Power generation from ambient humidity using protein nanowires,” *Nature* , vol. 578, no. 7796, pp. 550–554, Feb. 2020, doi: 10.1038/s41586-020-2010-9. [74] S. Chaurasia, R. Kumar, T. Tabrizzadeh, G. Liu, and K. Stamplecoskie, “All-Weather-Compatible Hydrovoltaic Cells Based on Al₂O₃ TLC Plates,” *ACS Omega* , vol. 7, no. 3, pp. 2618–2623, Jan. 2022, doi: 10.1021/acsomega.1c04751. [75] X. Gao *et al.* , “Electric power generation using paper materials,” *J Mater Chem A Mater* , vol. 7, no. 36, pp. 20574–20578, 2019, doi: 10.1039/c9ta08264f. [76] B. Shao *et al.* , “Bioinspired Hierarchical Nanofabric Electrode for Silicon Hydrovoltaic Device with Record Power Output,” *ACS Nano* , vol. 15, no. 4, pp. 7472–7481, Apr. 2021, doi: 10.1021/acsnano.1c00891. [77] K. Radotić, A. Kalauzi, D. Djikanović, M. Jeremić, R. M. Leblanc, and Z. G. Cerović, “Component analysis of the fluorescence spectra of a lignin model compound,” *J Photochem Photobiol B* , vol. 83, no. 1, pp. 1–10, Apr. 2006, doi: 10.1016/j.jphotobiol.2005.12.001.

Hosted file

EEM-Supporting Information- 1.docx available at <https://authorea.com/users/833392/articles/1226393-hydrovoltaic-energy-harvesting-from-nut-shells>

Hosted file

SV-1.mp4 available at <https://authorea.com/users/833392/articles/1226393-hydrovoltaic-energy-harvesting-from-nut-shells>

Hosted file

SV-2.mp4 available at <https://authorea.com/users/833392/articles/1226393-hydrovoltaic-energy-harvesting-from-nut-shells>